Thermally-driven mesopore formation and oxygen release in delithiated NCA cathode particles†

Münir M. Besli,[ab] Alpesh Khushalchand Shukla,[c] Chenxi Wei,[d] Michael Metzger,[a] Judith Alvarado,[e] Julian Boell,[a] Dennis Nordlund,[d] Gerhard Schneider,[bf] Sondra Hellstrom,[a] Christina Johnston,[a] Jake Christensen,[a] Marca M. Doeff,*[e] Yijin Liu*[d] and Saravanan Kuppan*[a]

The structural integrity of layered Ni-rich oxide cathode materials is one of the most essential factors that critically affect the performance and reliability of lithium-ion batteries. Prolonged battery operation often involves repeated phase transitions, buildup of mechanical stresses, and could provoke thermal spikes. Such sophisticated chemo-thermo-mechanical interplay can cause performance degradation through structural disintegration of the cathode active materials (CAMs). Herein, we systematically investigate the thermal decomposition, fracture, and oxygen evolution of chemically delithiated $Li_{0.3}Ni_{0.8}Co_{0.15}Al_{0.05}O_2$ (NCA) particles upon heating from 25 °C to 450 °C using a number of advanced X-ray and electron probes. We observed a continuous reduction of the Ni oxidation state upon heating, as well as the release of oxygen from the NCA lattice that undergoes the thermally induced phase transformations. The release of oxygen also created numerous mesopores throughout the analyzed particles, which could significantly affect the chemical and mechanical properties of the electrode. In addition, intergranular and intragranular fracturing at elevated temperatures also contribute to the degradation of the NCA cathode under these conditions. Our investigation of the mechanical integrity at elevated temperatures provides a fundamental understanding of the thermally driven chemomechanical breakdown of the NCA cathode active materials.

Introduction

In order to enable high energy density and long cycle life batteries for electric vehicles or off-grid power storage systems, intensive research has been conducted on advanced and improved cathode materials. Among the vast number of novel cathode materials, layered Ni-rich oxides, $LiNi_{1-x-y}Co_xAl_yO_2$ (NCA) or $LiNi_{1-x-y}Co_xMn_yO_2$ (NCM), in particular, are the most promising for next-gen lithium-ion batteries (LIBs).[1] Despite their high capacities of 220 mA h g^{-1} and the potential to reach even higher capacities of >250 mA h g^{-1} when cycled to 4.6 V,[2,3] layered Ni-rich oxides still face some major limitations. A significant drawback of high Ni content layered oxides is their intrinsic instability in their delithiated state, which occurs because of the effect of cation mixing.[4–9] The similar radii of Li ions (0.76 Å) and Ni^{2+} ions (0.69 Å) enable Li^+/Ni^{2+} site exchange, *e.g.* the occupation of 3b Li^+ layer sites by Ni^{2+}.[8] This lattice disordering leads to the obstruction of Li diffusion pathways through electrostatic repulsion by Ni cations[10,11] and contraction of Li slabs,[11] ultimately resulting in reduced capacity, cycling instability, and limited rate capability.[9] A further major drawback of layered Ni-rich oxides in the delithiated state is the release of oxygen[12–14] through reduction of Ni^{4+} in the delithiated material especially at elevated temperatures. In comparison to cathode materials with lower Ni content (*e.g.*, NCM111), layered Ni-rich oxides (*e.g.*, NCA, NCM523, 622 or 811) release more oxygen at lower onset temperatures accompanied with greater heat generation;[15–17] thus, Ni-rich cathodes are thermally less stable.[18] Several X-ray diffraction studies have shown that heat induced oxygen release in NCA and NCM takes place through structural changes of the material.[19–21] The layered oxide ($R\bar{3}m$) transitions first to a spinel ($Fd\bar{3}m$) then to a rock salt ($Fm\bar{3}m$) phase with rising temperature.[17,19,22] More oxygen is released during the transition from spinel to rock salt than for the first phase change. It is important to note that, due

[a]*Robert Bosch LLC, Research and Technology Center, Sunnyvale, California 94085, USA. E-mail: saravanan.kuppan@us.bosch.com*

[b]*Dept. of Mech. Engineering, Karlsruhe Institute of Technology (KIT), Karlsruhe 76131, Germany*

[c]*National Center of Electron Microscopy, Molecular Foundry, Lawrence Berkeley National Laboratory, Berkeley, California 94720, USA*

[d]*Stanford Synchrotron Radiation Lightsource, SLAC National Accelerator Laboratory, Menlo Park, California 94025, USA. E-mail: liuyijin@slac.stanford.edu*

[e]*Lawrence Berkeley National Laboratory, Energy Storage and Distributed Resources Division, University of California, Berkeley, California 94720, USA. E-mail: mmdoeff@lbl.gov*

[f]*Materials Research Institute, Aalen University, Aalen 73430, Germany*

† Electronic supplementary information (ESI) available. See DOI: 10.1039/c9ta01720h

to the hierarchically complex nature of the secondary particles, these phase transitions take place over a broad temperature range and co-exist within the particles with heterogeneous spatial distributions. Hence, it is of utmost importance to fully understand morphological changes happening upon thermal degradation of delithiated NCA materials in order to enable a safe operation of lithium-ion batteries.

For this work, we systematically studied the morphological defects in secondary delithiated $Li_{0.3}Ni_{0.8}Co_{0.15}Al_{0.05}O_2$ ($Li_{0.3}$NCA) particles that have gone through a serious temperature excursions. Our comprehensive study employs thermogravimetric analysis combined with mass spectrometry (TGA-MS), temperature controlled X-ray diffraction (T-XRD), hard and soft X-ray absorption spectroscopy (XAS), *in situ* two-dimensional nanoscale full-field (FF) transmission X-ray microscopy (TXM), and focused ion-beam-scanning electron microscopy (FIB-SEM). It aims to simplify the multitude of simultaneous influences on the secondary NCA particle fracturing during electrochemical cycling by investigating only the isolated temperature effect on the materials' morphology while simultaneously analyzing structural changes, oxygen evolution, and oxidation state changes. Our experimental results suggest that the charged NCA cathode undergoes complex structural and chemical evolution at elevated temperatures, involving the development of microporosity, particle cracking, local phase transformation, and oxygen evolution. Such an interconnected chemo-thermo-mechanical interplay has bearing upon the performance of the materials under a variety of operating conditions, including, but not limited to thermal abuse.

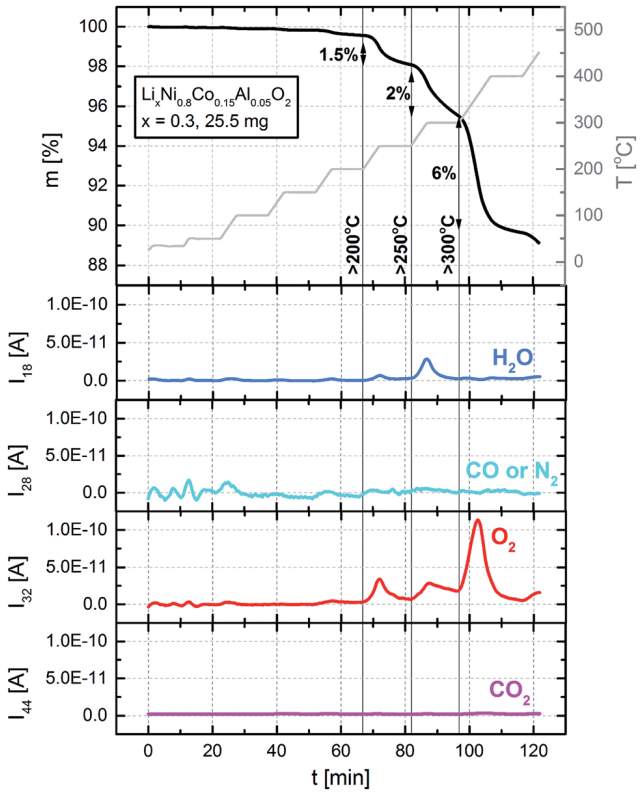

Fig. 1 TGA-MS data of $Li_{0.3}$NCA powder. Delithiated samples were heated to 300 °C in 50 °C steps with a 10 °C min^{-1} rate (grey). Temperature was hold for 10 minutes at each step. After reaching 300 °C, samples were heated in 100 °C steps up to 450 °C. Sample mass loss (black) and evolution of H_2O, CO (or N_2), O_2 and CO_2 gases (blue, cyan, red, and purple) were monitored during the heating process.

Results and discussion

TGA-MS

Thermogravimetric analysis combined with mass spectrometry (TGA-MS) was carried out using chemically delithiated $Li_{0.3}Ni_{0.8}Co_{0.15}Al_{0.05}O_2$ powder (here referred to as $Li_{0.3}$NCA) in the absence of any binder, carbon additive, or electrolyte. Electrode components other than the active material were excluded from our analysis to avoid complications from their contributions to the $Li_{0.3}$NCA thermal behavior and morphological changes. Fig. 1 shows the heating profile from 25 °C to 450 °C (grey curve), the associated mass loss (black curve) and the evolution of O_2, H_2O, and CO_2 (red, blue, purple, respectively). Overall, the sample lost ~12 wt% of its initial mass during heating to 450 °C. The MS data reveals that the weight loss mainly coincides with the release of O_2. At the transition from 200 to 250 °C and 250 to 300 °C only minor quantities of O_2 and H_2O are released, which account for 1.5 and 2.0 wt% mass loss, respectively. The majority of O_2 gas is released at the transition from 300 to 400 °C. This major O_2 evolution corresponds to a weight loss of approx. 6 wt% of the sample mass, which can be easily quantified due to the absence of other mass signals in this temperature range. Various onset temperatures of significant oxygen release have been reported in the literature such as 130 °C for NCM811,[17] 180 °C for charged $Li_{0.33}$NCA[19] and around 200 °C for charged $Li_{0.1}$NCA.[23] Our results indicate an onset temperature for oxygen release of 200 °C for $Li_{0.3}$NCA. A high level of dryness of the investigated sample can be assumed, since the MS data shows no H_2O release at around 100 °C, which would be attributed to physisorbed water. It was shown previously that LiOH powder decomposes to Li_2O *via* $2LiOH \rightarrow Li_2O + H_2O$ at 400 °C in Ar.[24] LiOH surface contaminants or –OH groups on NCA's oxide surface may, however, decompose at a lower temperature. Hence, the H_2O release at the 200 to 250 °C and 250 to 300 °C transitions could originate from LiOH impurities or –OH groups on the surface of the sample.[25] There are no quantifiable amounts of CO_2 released during heating to 450 °C. Li_2CO_3 was shown to decompose only at 700 °C.[24] Thus, it is not possible to make a statement about the presence of Li_2CO_3 impurities on the NCA surface.

Temperature controlled XRD

An *in situ* temperature controlled XRD study was carried out to systematically investigate the absolute thermal behavior of delithiated NCA. T-XRD allows information to be obtained on the bulk structural changes during thermal stress. Fig. 2 shows a series of T-XRD patterns of $Li_{0.3}$NCA continuously heated to 450 °C and subsequently cooled to 25 °C. No significant changes to the rhombohedral structure ($R\bar{3}m$) of delithiated NCA were detected below 150 °C, and the obtained

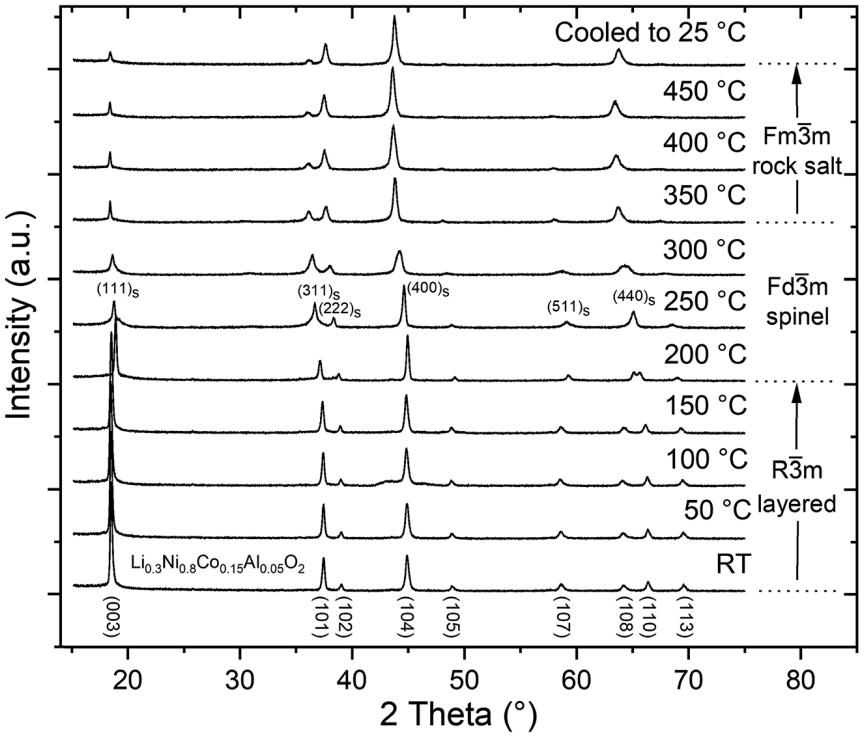

Fig. 2 Temperature controlled XRD patterns of $Li_{0.3}$NCA powder upon heating to 450 °C. $Li_{0.3}$NCA powder was heated from 25 °C to 450 °C in 50 °C increments. At each increment, the temperature was held and XRD spectrum was collected. Visible peak ratio variations and shifts indicate a phase transition from layered ($R\bar{3}m$) to spinel ($Fd\bar{3}m$) and spinel to NiO-type rock salt ($Fm\bar{3}m$).

diffraction patterns are in good agreement with XRD data reported in literature.[19,26] Upon further heating, we observed a phase transition from the layered to the disordered spinel phase ($R\bar{3}m$ to $Fd\bar{3}m$) starting at about 200 °C completed at about 250 °C. This phase transformation is indicated by the conjoining of the (108) and (110) peaks and decrease in the intensity ratio between the (003) and (104) peaks of the rhombohedral structure. These changes indicate that a significant number of cations (Ni, Co and Al) have migrated from the transition metal layer to the Li layer upon heating to about 250 °C. Subsequently, a second phase transitioning from the spinel to the NiO-type rock salt phase ($Fd\bar{3}m$ to $Fm\bar{3}m$) takes place at temperatures above 250 °C as marked by the decrease in $(311)_s$ and $(511)_s$ spinel peak intensities. This phase transition is accompanied by a major oxygen loss, correlating with the biggest oxygen loss observed in our TGA-MS results (Fig. 1). The intensities of the spinel phase peaks reached a maximum at about 300 °C, then declined to a very low level at 450 °C indicating that the spinel to rock salt phase transition continued until 450 °C under these conditions. This is in very good agreement with the TGA-MS data since the majority of O_2 releases at an onset temperature of 300 °C. We observed a majority of rock salt phase with minor spinel phase present at 450 °C and after cooling to 25 °C.

Soft and hard XAS analysis

Soft X-ray absorption spectroscopy (XAS) probes the changes in the oxidation state of elements as a function of the depth and, hence, is a vital tool for understanding changes in the valence state of various elements within the surface and sub-surface region. The depth profiling from surface to sub-surface can be achieved by varying the detection modality, namely the electron and fluorescence yield. The smaller mean free path length of electrons offers surface sensitive information (Auger Electron Yield, ~2 nm (AEY), Total Electron Yield ~5 nm (TEY)); whereas, the larger escape depth of photons (Fluorescence Yield, ~50 nm (FY)) offers sub-surface details of the sample.[27] The transition metal L-edge spectra (Ni and Co) are based on dipole allowed transitions starting at the $p_{1/2}$ and $p_{3/2}$ energy levels into the empty 3d orbitals (e_g^*). Due to spin–orbit coupling of the core hole, the L-edge spectrum is split into two well separated energy bands namely, the L_3 edge ($2p_{3/2}$) and the L_2 edge ($2p_{1/2}$). Furthermore, 2p–3d interactions and crystal field effects result in the splitting of these bands into multiplet structures. The shape, energy position, and branching ratio ($L_{3,high}/L_{3,low}$) of the multiplets contain information about the valence state, the spin state, and symmetry of the metal coordination of the samples. Therefore, any changes observed to the multiplet before and after the heat treatment process indicates the valence state changes during the heating process. Fig. 3c shows the normalized Ni L-edge spectra obtained using sub-surface (FY) and surface (TEY) sensitive modes. A significant change was observed in the Ni L-edge spectrum before and after heat treatment. The calculation of $L_{3,high}/L_{3,low}$ ratios shows Ni valence reduction at both probing depths as depicted in Fig. 3d. In order to quantify this reduction, we have measured several Ni

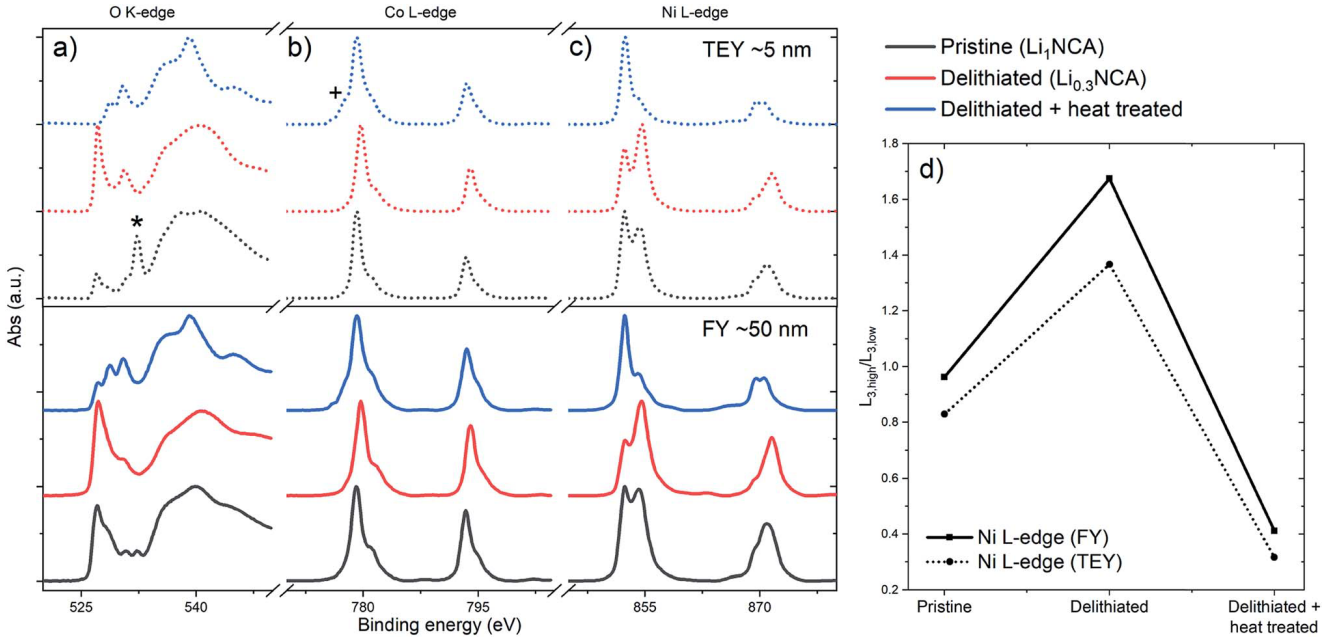

Fig. 3 (a–c) Soft XAS O K-edge, Co L-edge and Ni L-edge spectra for pristine (Li_1NCA), delithiated ($Li_{0.3}$NCA), and delithiated + heat-treated NCA powders in TEY (5 nm) and FY (50 nm) modes. (d) Calculated Ni $L_{3,high}/L_{3,low}$ ratios for all samples shown in TEY and FY mode. Peak marked with an asterisk in (a) is associated with Li_2CO_3. Plus sign in (b) is indicating slight reduction in Co.

containing oxide standards, namely NiO, NCM111, NCM622, NCM811 and NCA and linked the calculated $L_{3,high}/L_{3,low}$ ratio to their respective oxidation state (see ESI Fig. S1†). After linear fitting of the ratios to the oxidation states, the resulting correlation allows us to estimate the oxidation state of Ni in $Li_{0.3}$NCA heated to 450 °C using the calculated $L_{3,high}/L_{3,low}$ ratios of the TEY signals to 2.06+. This indicates a very severe reduction of Ni in the layered oxide to the level of rock salt (NiO) and also suggest that there is probably not much Li in the rock salt structure. Fig. 3b shows the normalized Co L-edge XAS spectra. In contrast to the Ni L-edge spectra, the TEY and FY modes show very minor changes, which illustrates that Co ions are less prone to reduce than the Ni ions during heating. However, a small peak that appears in the TEY and FY spectra for heat-treated $Li_{0.3}$NCA (marked with a plus sign) indicates slight reduction of Co^{3+} to Co^{2+}. Fig. 3a also shows the O K-edge spectra of the $Li_{0.3}$NCA before and after heat treatment. The intense absorption peak around 527.2 eV is associated with the lattice oxygen (metal–oxygen bond) in the layered oxide (oxygen 1s → metal 3d orbitals hybridized with O 2p). The broad peak features above 534 eV correspond to the O 2p → Ni 4sp transitions and other empty orbitals in this energy region. The peak observed at 532.3 eV (marked with an asterisk) in the surface sensitive mode (TEY) is associated with Li_2CO_3, which is often found on surfaces of layered Ni-rich oxide materials.[28,29] Since Li_2CO_3 is mostly found on the outmost surface of the particle, the corresponding peak appears only in TEY mode (5 nm). During the delithiation process, the native Li_2CO_3 layer on the pristine NCA surface is washed away, resulting in an amplification of the lattice oxygen peak at 527.2 eV. As seen in the Ni L-edge spectra, there is a significant change observed in the O K-edge spectra in both the surface and sub-surface regions upon heat treatment. We note the remarkable decrease in the lattice oxygen peak at 527.2 eV and evolution of the peak at 539.2 eV, which is attributed to the formation of divalent Ni at the surface and sub-surface. These observations indicate that NiO is formed at the surface and sub-surface upon heat treatment, consistent with the TGA-MS and T-XRD results.

In addition to the surface analysis, we conducted hard X-ray absorption spectroscopy (XAS), which correlates the changes in the absorption edge to the changes in the average oxidation state of the absorbing atoms in the bulk material.[19,30,31] For example, a forward shift (higher eV) in edge energies indicates an increased valence state of the atom being probed. Since the core electrons are more strongly bound to the nucleus in the higher valence state, their photo-ionization requires higher photon energies, whereas a backward shift (lower eV), in contrast, indicates a decreased valence state. Fig. 4 shows the normalized Ni K-edge X-ray absorption near edge structure (XANES) spectra for pristine, delithiated (+heat-treated) NCA, and also NiO (shown as a reference). While Ni is divalent in NiO and trivalent in pristine NCA, the oxidation state of Ni in delithiated NCA is estimated to be close to 3.7+, under the assumption, that most of the charge compensation is done by Ni.[32] Using the edge position defined by the photoelectron energy origin (E_0),[33] we quantified the changes happening for delithiated heat-treated NCA (450 °C), in relation to pristine NCA (Li_1NCA) and delithiated NCA ($Li_{0.3}$NCA). Additionally, the linear relationship between the Ni K-edge energy and state of charge (SOC) makes it possible to use the determined Ni oxidation state as a proxy for pseudo SOC estimations as reported in literature.[34–38] While the edge energy for heat-treated

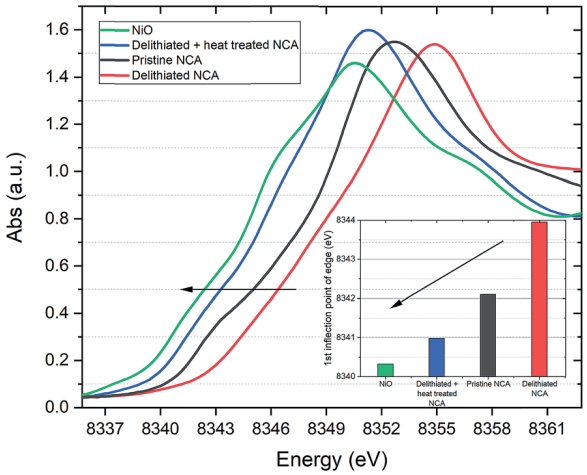

Fig. 4 Normalized Ni K-edge XANES spectra of (black) delithiated $Li_{0.3}$NCA, (blue) pristine NCA, (red) delithiated and heat-treated NCA, (green) NiO obtained in transmission mode. Retrieved data reflects the oxidation state of the bulk material. The edge position of NiO is used as a reference for Ni^{2+}. The inset shows the edge energies derived from the 1st inflection point of the spectra.

$Li_{0.3}$NCA is 8340.98 eV, the edge energies of pristine NCA and $Li_{0.3}$NCA are 8342.10 eV and 8343.95 eV, respectively. Edge energies were derived from the 1st inflection point of each spectra. The entire Ni K-edge clearly shifts from higher to lower energies in the order of delithiated, pristine, and delithiated + heat-treated NCA, indicates a strong reduction in the Ni oxidation state upon heating. This strong edge shift (2.97 eV) between $Li_{0.3}$NCA and heat-treated $Li_{0.3}$NCA illustrates that the average oxidation state of Ni decreases significantly to compensate for the oxygen released from the delithiated $Li_{0.3}$NCA during thermal excursion. The XANES result is in complete agreement with our TGA-MS, T-XRD and previous works.[19,39,40] It has also been demonstrated that the oxygen release and crystal structure phase-change are correlated.[19] Furthermore, it is believed that the phase transitioning from layered to rock salt predominantly affects the surface of secondary NCA particles while the core of the material still remains as a layered oxide.[41] However, recently Zhang *et al.* have shown phase transitions can occur below the surface. Using transmission electron microscopy (TEM) they demonstrated how rock salt domains within the core of the material initiate degradation phenomena such as intragranular cracks.[42,43] Hence, it is of utmost importance to understand the interplay of the observed effects such as oxygen evolution, phase transition and reduction in further detail. In order to do so, we have conducted a series of imaging measurements to obtain chemical and morphological insight into decrepitation of secondary particles.

2D-FF-TXM

Two-dimensional full-field transmission X-ray microscopy (2D-FF-TXM) was used to visualize the lateral spatial distribution of the Ni oxidation state over an isolated secondary $Li_{0.3}$NCA particle upon *in situ* thermal treatment to 450 °C. Using the beamline 6-2c of the Stanford Synchrotron Radiation Lightsource (SSRL), a series of 2D Ni K-edge XANES maps were collected as a function of the temperature (see Fig. 5a–h). Note that the 2D projections of spherical particle represent the averaged oxidation state over the depth of the spherical particle. The spatial distribution of the Ni valence state exhibits continuous overall reduction with increasing temperature as indicated by the evolution of the color-coded maps in Fig. 5a–h. The heterogeneity in the maps, on the other hand, highlights the complexity of the reaction at the mesoscale,[44] where the grain boundaries and defects are populated. For better capturing the dynamic evolution of the thermally driven chemical evolution, we calculated the differential 2D Ni K-edge energy maps, as shown in Fig. 5i–o. Two critical temperature transitions are apparent on the calculated differential maps, namely the 200–250 °C and the 300–350 °C regions (Fig. 5l and n). These differential maps show dark blue coloring and represent a strong negative shift of the Ni K-edge energy, which indicates a significantly higher degree of reduction that happened when transitioning from 200 to 250 °C and from 300 to 350 °C. To confirm our interpretation of the visualized maps (Fig. 5a–o), we plotted the probability distribution of the Ni K-edge energy and the differential energies of the XANES maps in Fig. 5p and q, respectively. Fig. 5p confirms a monotonic reduction of Ni upon heating while highlighting two of the major shifts toward lower energies that appear upon heating from 200 to 250 °C and from 300 to 350 °C. Similar to this, the probability distributions in the differential maps offer comparable information. It is interesting to point out that there are positive components in the probability distribution of the differential maps, which could be attributed to the thermally driven lithium redistribution within the secondary particle, a phenomenon that has been reported in NCM compounds.[45] The highlighted temperature transitions are in very good agreement with our TGA-MS and T-XRD data. The TGA-MS shows the most significant oxygen evolution at the same temperature transitions at which the XRD data shows a phase change. Also in accordance with our XAS data, a clear reduction of Ni is visible upon heat treatment that seems to be happening homogenously throughout the particle.

Particle morphology

In a final step, we investigated morphological changes upon heating on a single particle level using scanning electron microscopy (SEM) and focused ion-beam-scanning electron microscopy (FIB-SEM). Several delithiated, as well as delithiated and heated treated particles (450 °C), were subjected to a surface SEM study and FIB-SEM tomography to highlight morphological changes throughout the particle and visualize the impact of oxygen evolution on the core, sub-surface, and surface of the particle. Fig. 6 shows a representative example of the conducted surface SEM study for a delithiated NCA particle.

None of the analyzed delithiated NCA particles showed mesopores on the surface even in images taken at higher magnifications as shown in Fig. 6b. Chemical delithiation is widely used to prepare delithiated cathode materials similar to

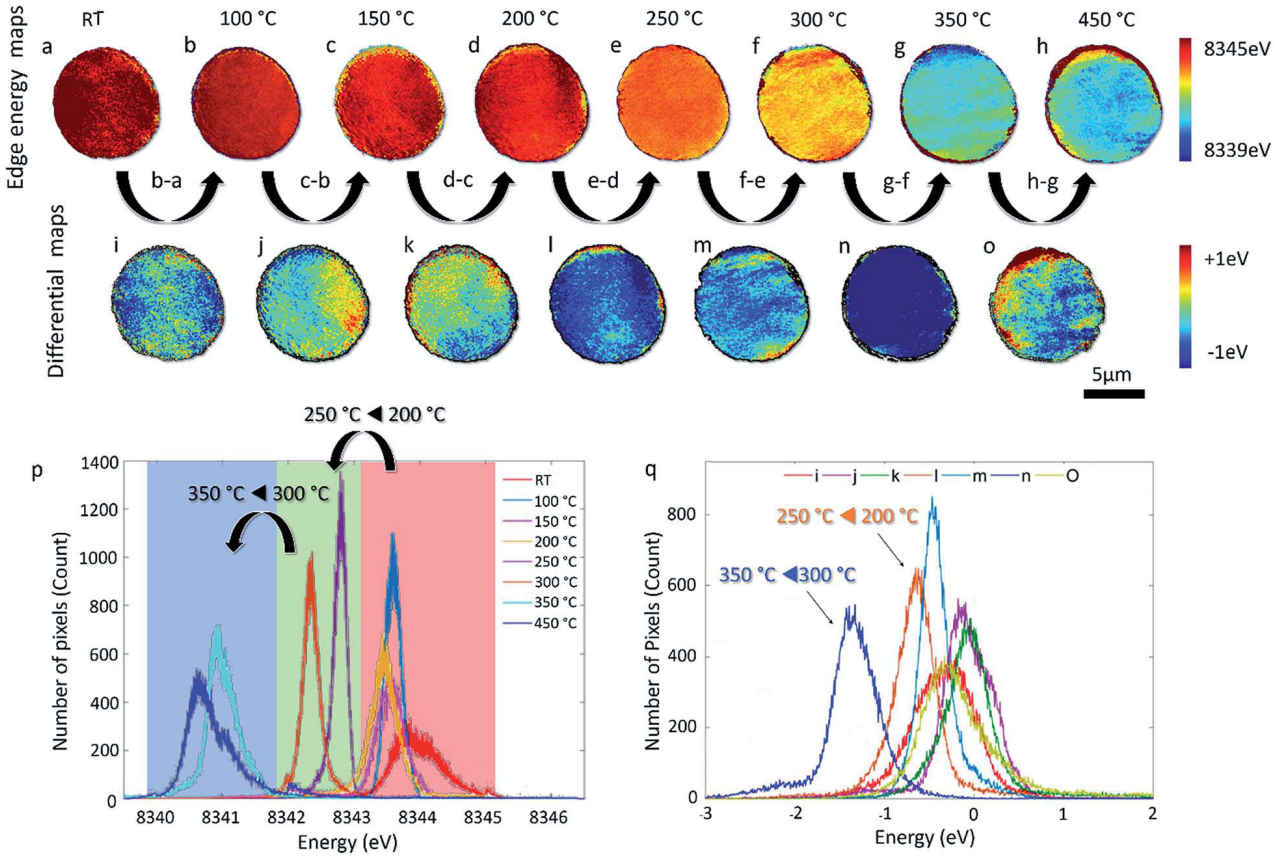

Fig. 5 *In situ* 2D Ni K-edge XANES mapping over an arbitrarily selected NCA particle upon thermal treatment. Panels (a–h) show the evolution (reduction) of the Ni oxidation state. The corresponding energy distributions of panels (a–h) are shown in panel (p), highlighting two critical temperature transitions (200–250 °C and 300–350 °C), which is in good agreement with oxygen evolution observed in Fig. 1 and phase transitions in Fig. 2. Panels (i–o) show the differential Ni K-edge energy maps, suggesting that the internal redistribution of Li occurs concurrently with the overall Ni reduction. The corresponding energy distributions of panels (i–o) are shown in panel (q).

electrochemically charged cathode, it often involves strong chemical oxidants *e.g.*, nitronium tetrafluoroborate (NO_2BF_4) with very high potentials (~5.1 V *vs.* Li^+/Li).[35] Under these conditions, delithiated secondary NCA particles are fully intact but show slight intergranular cracking similar to electrochemically delithiated NCA.[46,47] In contrast to particles that were only delithiated, delithiated and heat-treated (450 °C) particles show extensive mesopores on their surface. Fig. 7 shows the surface of a heat-treated, delithiated particle.

The observed evolution of mesopores upon heat treatment strongly suggest that oxygen escapes the surface *via* mesopores under thermal abuse conditions (more images are shown in ESI Fig. S2†). This is significantly different from electrochemical cycling-induced surface degradation of layered Ni-rich oxides involving reaction of the cathode surface with the electrolyte and surface oxygen loss. The latter has been shown to cause stronger electrolyte decomposition than purely potential driven electro-oxidation of electrolyte, since singlet oxygen is released

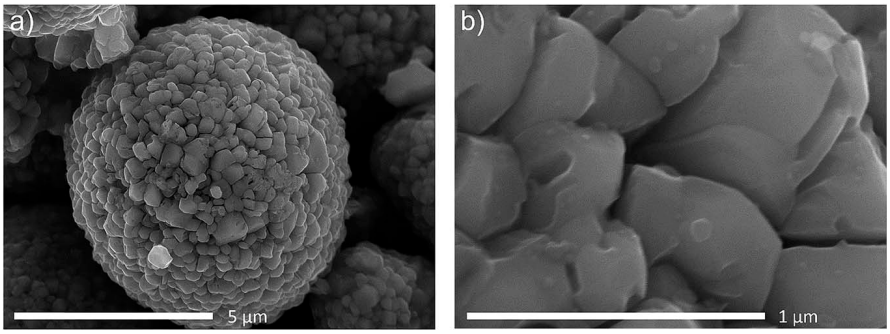

Fig. 6 (a) Surface of a delithiated NCA particle. (b) Magnified area of the same particle surface shown in (a). While small defects, introduced by the chemical delithiation process are visible, no other morphological changes are present.

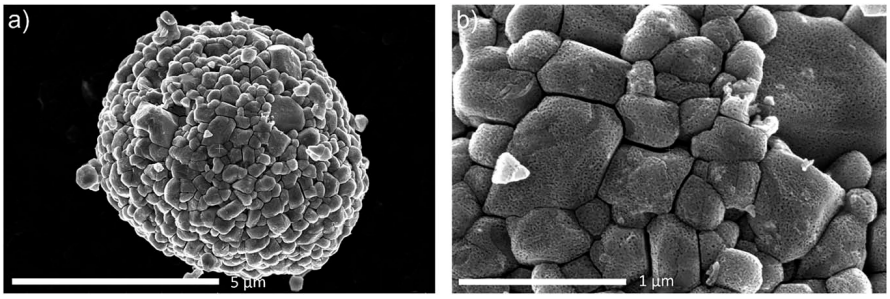

Fig. 7 (a) Surface of a delithiated and heat-treated NCA particle. (b) Magnified area of the same particle surface shown in (a). Besides small morphological changes introduced by chemical delithiation, an extensive amount of uniformly distributed mesopores are visible on the surface.

from the cathode surface at ~80% delithiation of layered oxides reacts readily with electrolyte.[12,48–50] Potential induced oxygen loss starts at the surface and sub-surface region, while the bulk mainly stays intact.[51–53] In this so-called core–shell model, the degradation of layered oxide materials is initiated by a transition from a layered phase to a spinel phase. Ultimately, the surface of the secondary particle transforms to the rock salt phase, the sub-surface to a spinel phase, while the majority of the core remains in the layered phase.[51,53–56] In the absence of electrolyte, as in our study, the observed mesopores clearly show the evolution of oxygen from the surface as a result of thermal abuse.

In order to see if mesopores from oxygen release are also present in the core of thermally treated and delithiated secondary NCA particles, we milled many secondary particles using a focused ion-beam. Fig. 8 shows a representative SEM image showing the cross-section of a milled particle.

Particle cross-sectioning highlights that mesopores are present ubiquitously throughout the bulk of the particle (see ESI Fig. S3, S5 and Video S2†). Upon closer observation besides intergranular cracks, also a few intragranular cracks are present within primary particles, which show a parallel alignment in some of the primary grains (see ESI Fig. S3f, S4d and S5d†). Further, we noticed a widespread appearance of mesopores appearing preferably along intragranular cracks. Pengfei *et al.* have observed that intragranular cracks in overcharged NCM111 are predominantly parallel and propagate along the (003) plane,[57] which might be similar in delithiated and heat treated NCA. While reduction of Ni upon phase-transitioning and the accompanying oxygen release has been widely reported in the literature,[12,50,51,56,58,59] the evolution of mesopores in entire particles has not been reported yet to the best of our knowledge. All FIB-SEM images reported here were obtained on delithiated NCA that was heated to 450 °C. We repeated the experiment using different temperatures in order to find out the critical temperature at which the mesopores development is initiated. Four batches of delithiated NCA material were individually heated to 150 °C, 250 °C, 350 °C or 450 °C, using a similar temperature program as for the TGA-MS and XRD experiments and observed in the SEM. Our SEM investigations showed that the evolution of pores starts at 350 °C (see ESI Fig. S4†). This is in good agreement with our TGA-MS results (Fig. 1) and 2D-FF-TXM results (Fig. 5).

Besides the observed evolution of mesopores throughout the bulk of the particle, upon thermal treatment, crack volumes for delithiated particles seem to shrink due to the evolution of mesopores (see ESI Fig. S5†). To see how mesopores affect the intergranular crack volume, we look at 2D slices of the NCA particles with fixed cross-sectional area before and after heat treatment (see Fig. 9) and compare black area (cracks) to white area (solid phase). A machine-learning based segmentation was deployed using Trainable Weka Segmentation.[60] Several 2D slices of delithiated NCA particles and heat-treated NCA particles were used to train the machine-learning algorithm. The algorithm was then used to calculate the crack area in the 2D slices (shown in black) resulting from a change in the volume fractions of intergranular cracks and mesopores for delithiated particles and heat-treated delithiated NCA particles. Although

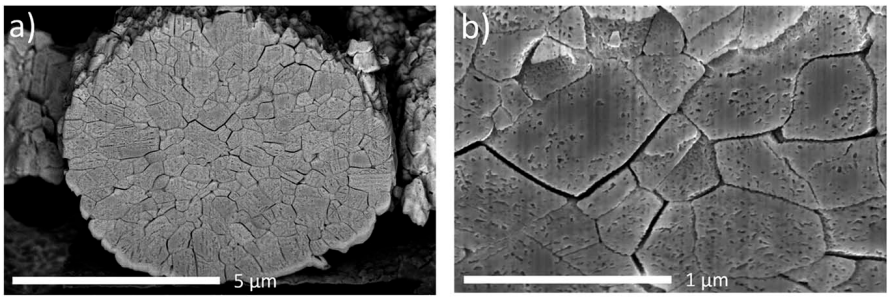

Fig. 8 (a) Cross-sectional SEM image for a secondary NCA particle after focused ion-beam milling. Cross-section of particle indicates a homogenous distribution of mesopores within the particle core. (b) High magnification of the cross-section shown in (a).

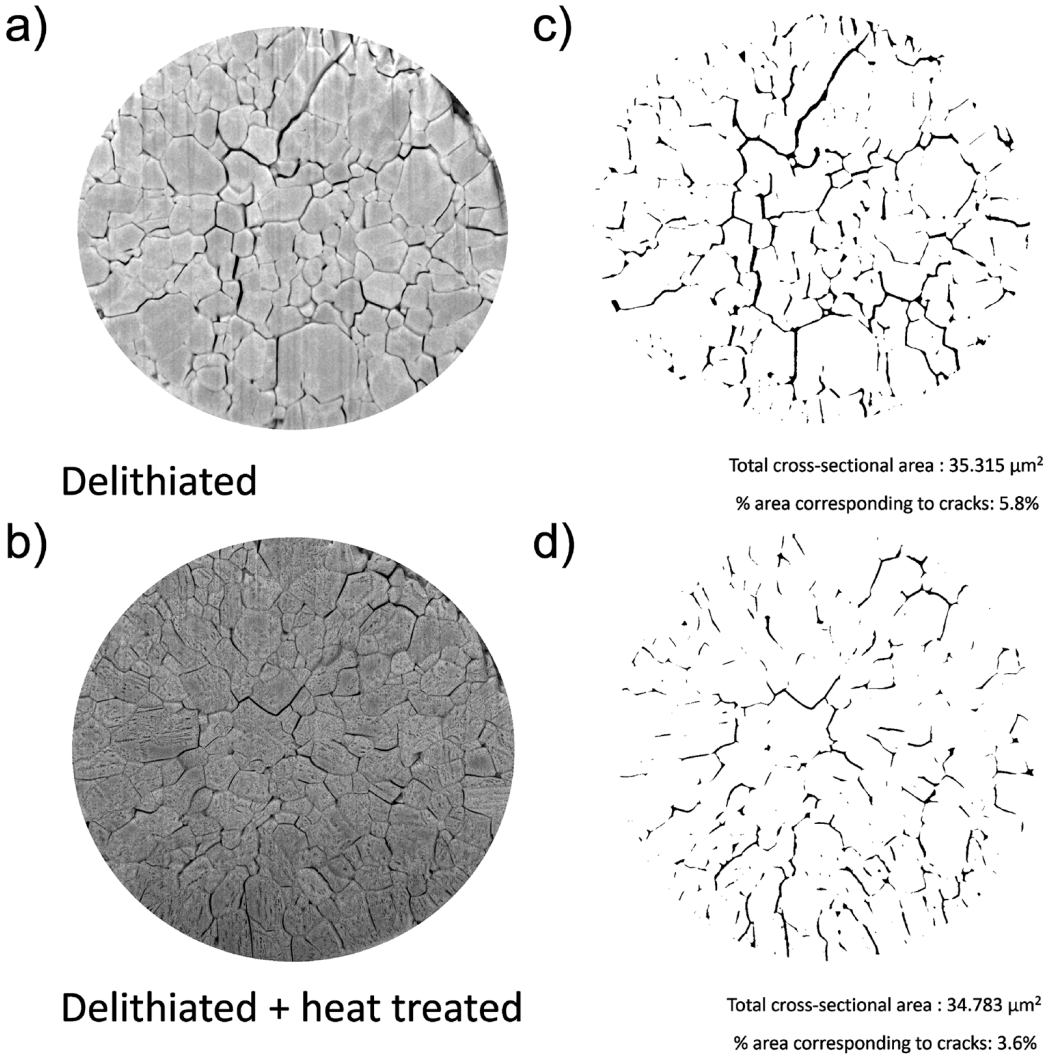

Fig. 9 (a and b) Cross-sections of a delithiated and heat-treated delithiated NCA particle of similar total cross-sectional areas used to determine crack area using a machine learning algorithm, respectively. (c and d) Binary maps for the calculated crack area for the respective particle shown in (a) and (b).

we just obtain quantitative information about the crack area in a 2D slice of the NCA particles, it is reasonable to assume that a larger crack area also implies a larger crack volume fraction, as long as we compare two slices with same cross-sectional area. Interestingly, when comparing delithiated and heat-treated delithiated NCA particles with similar cross-sectional areas, the total crack area of heat-treated NCA particles is smaller than that of the delithiated particles (Fig. 9c and d). This indicates that mesopore evolution results in increased void volume within primary particles and thus decreased crack volume within the secondary agglomerate. The expansion of primary grains has been quantified for milled particles with very similar total cross-sectional areas (Fig. 9) and shows a significant reduction of the total crack area from 5.8% (delithiated particle) to 3.6% (heat-treated delithiated particle). This calculation was repeated two more times for pairs of delithiated, and delithiated and heat-treated secondary NCA particles with similar cross-sectional area. On average, calculated crack area for delithiated particles resulted in 5.33%, while delithiated particles showed a crack area of 3.99% after heat-treatment. Even though the crack area change cannot be directly translated into a change in the crack volume fraction, we attempted to calculate the volume fraction that is associated with the mesopores by using an 'apparent crack volume' obtained from the 2D binary maps in Fig. 9c and d and the mass loss shown in Fig. 1. The details of the calculation can be found in the ESI.† While the result is quite sensitive to the density of the different NCA phases after heat treatment, we can get an idea of the mesopore volume. Assuming that the NCA particles after heat treatment consists of a delithiated layered phase, a disordered rock salt phase, intergranular cracks and mesopores, the mesopore volume fraction would be between 10 and 20%.

Conclusion

In this paper, we have employed a variety of techniques to thoroughly probe chemical and morphological changes of chemically delithiated NCA cathode active material that was

continuously heated to 450 °C. Our findings indicate oxygen evolution, phase transitioning, and continuous reduction of surface, sub-surface, and bulk Ni, and inter- as well as intragranular cracking and the creation of mesopores upon heating. While our work is in good agreement with what has been reported previously in the literature for the thermal degradation of delithiated NCA, it further reveals that oxygen evolution causes mesopores upon heating to temperatures above 350 °C, creating a pathway for release of lattice oxygen from the bulk and surface. To the best of our knowledge, this has not been reported before. Furthermore, we observed, that some of the mesopores seem to follow intragranular cracks, that appear in somewhat parallel manner within primary grains. These mesopores most probably are part of the compensation of the internal pressure build up due to oxygen evolution. However, internal pressure build up further decreases the volume of intergranular cracks suggesting that mesopores lead to a volume expansion of primary grains. While the chemical and morphological changes appear at temperatures higher than 200 °C, delithiated NCA shows good short term stability for temperatures up to 200 °C.

Experimental procedures

Chemical delithiation

Pristine NCA ($Li_1Ni_{0.8}Co_{0.15}Al_{0.05}O_2$) cathode active material, of commercial grade, was chemically delithiated to $Li_{0.3}Ni_{0.8}Co_{0.15}Al_{0.05}O_2$ through oxidation with a 0.1 M solution of nitronium tetrafluoroborate (NO_2BF_4) in acetonitrile. The delithiated NCA powder was subsequently dried in a vacuum oven at room-temperature. The Li ratio in NCA is governed by the ratio of NCA to NO_2BF_4 during the oxidation reaction and the elemental stoichiometry was subsequently determined *via* inductively coupled plasma-optical emission spectroscopy (ICP-OES) to $Li_{0.30}Ni_{0.8}Co_{0.15}Al_{0.05}O_2$.

Materials characterization

Thermogravimetric analysis of delithiated NCA powder was performed on a TA Instruments TGA 5500 instrument coupled to a TA Instruments Discovery benchtop quadrupole mass spectrometer for evolved gas analysis. 25.5 mg of delithiated NCA powder was weighed in a stainless steel crucible and transferred to the TGA-MS instrument with minimal exposure to ambient air. After sample insertion, the furnace was purged with Ar for 30 min at 25 °C to minimize trace amounts of ambient air during the measurement. The active material sample was heated from 25 °C to 450 °C at 10 °C min^{-1} with 10 min hold times at several discrete temperatures. Mass spectrometer was operated in multiple ion detection mode and recorded m/z of 2, 18, 19, 28, 32, 44 ions with a <10 s time resolution. Note that the $Li_{0.3}$NCA powder was stored in a glovebox and the sample was transferred to the TGA-MS instruments in a closed container without exposure to ambient air.

Temperature controlled XRD analysis was performed on a Panalytical X'Pert Pro diffractometer with monochromatized Cu K_α radiation equipped with an Anton Parr HTK 1200 hot stage. Scans were collected between 15 and 75° (2θ) at a rate of 0.0001° s^{-1} and a step size of 0.022°. Delithiated NCA powder was heated in air at a rate of 5 °C min^{-1} and the XRD patterns were recorded at a temperature step size of 50 °C with each temperature holding for 10 minutes before data collection.

Hard XAS data on Ni K-edge was collected in transmission mode using a Si (220) monochromator at SSRL beamline 4-1. Pristine NCA, as-prepared delithiated NCA as well as delithiated + heat-treated NCA and NiO powders were dispersed on Kapton films for the measurement. Higher harmonics in the X-ray beam were rejected by detuning the Si (220) monochromator by 40% at the Ni edge. Energy calibration was accomplished by using the first inflection points in the spectra of Ni metal foil reference at 8332.8 eV. XANES data were analyzed by Sam's Interface for XAS Package (SIXPACK),[61] with the photoelectron energy origin (E_0) determined by the first inflection point of the absorption edge jump.

For soft XAS measurements, a thin layer of the samples was spread onto a conductive carbon tape which was then attached to an aluminum sample holder inside an Ar-filled glovebox. Measurements for O K-edge, Co L-edge and Ni L-edge were carried out at the 31-pole wiggler beamline 10-1 at SSRL with a spherical grating monochromator with 20 mm entrance and exit slits, a 0.2 eV energy resolution and a 1 mm^2 beam spot. Data were collected at room temperature under ultrahigh vacuum (10^{-9} Torr) in a single load using the total electron yield (TEY) and fluorescence yield (FY) mode detectors.

2D-FF-TXM imaging was performed at the 54 pole wiggler beamline 6-2c at the SSRL. Detailed beamline configuration can be found in a previous report.[62] Delithiated NCA powder was carefully dispersed in cylindrical quartz capillaries (100 μm in diameter and 10 μm in wall thickness) and carefully mounted to the beamline sample holder. Slow and steady helium gas flow was applied to the capillaries to prevent air exposure. The X-ray energy was tuned to Ni K-edge and then focused onto the sample by an elliptically shaped capillary condenser providing illumination for a FOV of approx. 30 × 30 μm^2. 2D transmission images (0.5 s exposure time, 5 repetitions, binning 2, 1024 × 1024 pixels) were collected from 8313 to 8394 eV with a minimum step size of 1 eV. To remove distortions caused by the flux and beam instabilities, concurrent acquisition of reference images at each energy was also performed through an open area of the sample (outside the capillary) with the same imaging configuration. The repetitions in exposures were carried out to enhance the dynamic range of the existing charge-coupled device and, subsequently, improve the signal to noise ratio in the data. 2D-FF-TXM images were first acquired at room temperature, upon heating, images were acquired in 50 °C intervals from 100 °C to 350 °C and lastly at 450 °C.

FIB-SEM of delithiated and delithiated + heat-treated particles was performed using a Helios G4 dual-beam FIB. Heat-treatment protocol was adjusted to the same protocol used in our other experiments. Sectioning of particles was performed using gallium ions at 30 kV and were imaged using electrons at 5 kV. The currents used for ion and electron beams were 26 pA and 0.1 nA, respectively. Secondary electron as well as back-scattered electron detectors were used for imaging. Serial-

sectioning and SEM imaging was done every 10 nm and the images were aligned and reconstructed to create a 3D volume of entire secondary particles.

Author contribution

S. K. designed this work and prepared delithiated cathode for this study; M. M. B. and S. K. carried out *in situ* XRD, synchrotron XAS and SEM experiments. M. M. B. processed and visualized *in situ* XRD, soft and hard XAS, and surface SEM data. J. A. assisted with *in situ* XRD and D. N. assisted with soft XAS. M. M. performed and analyzed TGA-MS. C. W. and Y. L. performed *in situ* 2D-FF-TXM and analyzed the data. J. B. assisted with *in situ* 2D-FF-TXM. A. K. S. performed FIB-SEM experiments and conducted analysis using machine learning methods. M. M. B. prepared the figures and wrote the initial manuscript draft under the supervision of S. K. The results were discussed by M. M. B., A. K. S., M. M., J. A., G. S., S. H., C. J., J. C., M. M. D., Y. L. and S. K. All authors reviewed the manuscript and approved the final manuscript.

Conflicts of interest

There are no conflicts to declare.

Acknowledgements

The synchrotron experiments of this research were carried out at the SSRL, a Directorate of SLAC National Accelerator Laboratory and an Office of Science User Facility operated for the U.S. Department of Energy Office of Science by Stanford University. Use of the Stanford Synchrotron Radiation Lightsource, SLAC National Accelerator Laboratory, is supported by the U.S. Department of Energy, Office of Science, Office of Basic Energy Sciences under Contract No. DE-AC02-76SF00515. We thank Drs Erik Nelson and Matthew Latimer for assisting with the synchrotron experiments. The engineering support from D. Van Campen, D. Day and V. Borzenets for the TXM experiment at beamline 6-2C of SSRL is gratefully acknowledged. Work at the Molecular Foundry was supported by the Office of Science, Office of Basic Energy Sciences, of the U.S. Department of Energy under Contract No. DE-AC02-05CH11231.

References

1 S. T. Myung, F. Maglia, K. J. Park, C. S. Yoon, P. Lamp, S. J. Kim and Y. K. Sun, *ACS Energy Lett.*, 2017, **2**, 196–223.
2 W. Liu, P. Oh, X. Liu, M. J. Lee, W. Cho, S. Chae, Y. Kim and J. Cho, *Angew. Chem., Int. Ed.*, 2015, **54**, 4440–4457.
3 M. M. Thackeray, S.-H. Kang, C. S. Johnson, J. T. Vaughey, R. Benedek and S. A. Hackney, *J. Mater. Chem.*, 2007, **17**, 3112–3125.
4 T. Ohzuku, A. Ueda and M. Nagayama, *J. Electrochem. Soc.*, 1993, **140**, 1862–1870.
5 S. Zheng, R. Huang, Y. Makimura, Y. Ukyo, C. A. J. Fisher, T. Hirayama and Y. Ikuhara, *J. Electrochem. Soc.*, 2011, **158**, A357–A362.
6 Y. Cho, P. Oh and J. Cho, *Nano Lett.*, 2013, **13**, 1145–1152.
7 M. Jo, M. Noh, P. Oh, Y. Kim and J. Cho, *Adv. Energy Mater.*, 2014, **4**, 1301583.
8 J. Zhao, W. Zhang, A. Huq, S. T. Misture, B. Zhang, S. Guo, L. Wu, Y. Zhu, Z. Chen, K. Amine, F. Pan, J. Bai and F. Wang, *Adv. Energy Mater.*, 2017, **7**, 1601266.
9 P. Yan, J. Zheng, D. Lv, Y. Wei, J. Zheng, Z. Wang, S. Kuppan, J. Yu, L. Luo, D. Edwards, M. Olszta, K. Amine, J. Liu, J. Xiao, F. Pan, G. Chen, J. G. Zhang and C. M. Wang, *Chem. Mater.*, 2015, **27**, 5393–5401.
10 E. M. Erickson, F. Schipper, T. R. Penki, J.-Y. Shin, C. Erk, F.-F. Chesneau, B. Markovsky and D. Aurbach, *J. Electrochem. Soc.*, 2017, **164**, A6341–A6348.
11 K. Kang and G. Ceder, *Phys. Rev. B: Condens. Matter Mater. Phys.*, 2006, **74**, 094105.
12 R. Jung, M. Metzger, F. Maglia, C. Stinner and H. A. Gasteiger, *J. Electrochem. Soc.*, 2017, **164**, A1361–A1377.
13 S. M. Bak, K. W. Nam, W. Chang, X. Yu, E. Hu, S. Hwang, E. A. Stach, K. B. Kim, K. Y. Chung and X. Q. Yang, *Chem. Mater.*, 2013, **25**, 337–351.
14 H. Konishi, M. Yoshikawa and T. Hirano, *J. Power Sources*, 2013, **244**, 23–28.
15 I. Belharouak, W. Lu, D. Vissers and K. Amine, *Electrochem. Commun.*, 2006, **8**, 329–335.
16 I. Belharouak, W. Lu, J. Liu, D. Vissers and K. Amine, *J. Power Sources*, 2007, **174**, 905–909.
17 S. Bak, E. Hu, Y. Zhou, X. Yu, S. D. Senanayake, S. Cho, K. Kim, K. Y. Chung, X. Yang and K. Nam, *ACS Appl. Mater. Interfaces*, 2014, **6**, 22594–22601.
18 H. J. Noh, S. Youn, C. S. Yoon and Y. K. Sun, *J. Power Sources*, 2013, **233**, 121–130.
19 K.-W. Nam, S.-M. Bak, E. Hu, X. Yu, Y. Zhou, X. Wang, L. Wu, Y. Zhu, K.-Y. Chung and X.-Q. Yang, *Adv. Funct. Mater.*, 2013, **23**, 1047–1063.
20 W.-S. Yoon, O. Haas, S. Muhammad, H. Kim, W. Lee, D. Kim, D. A. Fischer, C. Jaye, X.-Q. Yang, M. Balasubramanian and K.-W. Nam, *Sci. Rep.*, 2015, **4**, 6827.
21 S. Bak, E. Hu, Y. Zhou, X. Yu, S. D. Senanayake, S. Cho, K. Kim, K. Y. Chung, X. Yang and K. Nam, *ACS Appl. Mater. Interfaces*, 2014, **6**, 22594–22601.
22 B. Xu, C. R. Fell, M. Chi and Y. S. Meng, *Energy Environ. Sci.*, 2011, **4**, 2223–2233.
23 Y. Huang, Y.-C. Lin, D. M. Jenkins, N. A. Chernova, Y. Chung, B. Radhakrishnan, I.-H. Chu, J. Fang, Q. Wang, F. Omenya, S. P. Ong and M. S. Whittingham, *ACS Appl. Mater. Interfaces*, 2016, **8**, 7013–7021.
24 H. Beyer, S. Meini, N. Tsiouvaras, M. Piana and H. A. Gasteiger, *Phys. Chem. Chem. Phys.*, 2013, **15**, 11025–11037.
25 R. Jung, R. Morasch, P. Karayaylali, K. Phillips, F. Maglia, C. Stinner, Y. Shao-Horn and H. A. Gasteiger, *J. Electrochem. Soc.*, 2018, **165**, A132–A141.
26 K. W. Nam, W. S. Yoon and X. Q. Yang, *J. Power Sources*, 2009, **189**, 515–518.
27 J. Stohr, *NEXAFS Spectroscopy*, Springer-Verlag, Berlin Heidelberg, 1992.

28 W.-S. Yoon, K. Y. Chung, J. McBreen, D. A. Fischer and X.-Q. Yang, *J. Power Sources*, 2006, **163**, 234–237.

29 J. Xu, E. Hu, D. Nordlund, A. Mehta, S. N. Ehrlich, X. Q. Yang and W. Tong, *ACS Appl. Mater. Interfaces*, 2016, **8**, 31677–31683.

30 Z. Gong and Y. Yang, *J. Energy Chem.*, 2018, **27**, 1566–1583.

31 Y. Terada, K. Yasaka, F. Nishikawa, T. Konishi, M. Yoshio and I. Nakai, *J. Solid State Chem.*, 2001, **156**, 286–291.

32 M. Balasubramanian, X. Sun, X. Q. Yang and J. McBreen, *J. Electrochem. Soc.*, 2000, **147**, 2903–2909.

33 K. Saravanan, A. Jarry, R. Kostecki and G. Chen, *Sci. Rep.*, 2015, **5**, 8027.

34 A. Manthiram, B. Song and W. Li, *Energy Storage Materials*, 2017, **6**, 125–139.

35 S. Kuppan, Y. Xu, Y. Liu and G. Chen, *Nat. Commun.*, 2017, **8**, 14309.

36 W.-S. Yoon, M. Balasubramanian, K. Y. Chung, X.-Q. Yang, J. McBreen, C. P. Grey and D. A. Fischer, *J. Am. Chem. Soc.*, 2005, **127**, 17479–17487.

37 C. Rumble, T. E. Conry, M. Doeff, E. J. Cairns, J. E. Penner-Hahn and A. Deb, *J. Electrochem. Soc.*, 2010, **157**, A1317–A1322.

38 J. Xu, F. Lin, M. M. Doeff and W. Tong, *J. Mater. Chem. A*, 2017, **5**, 874–901.

39 E. Hu, Y. Lyu, H. L. Xin, J. Liu, L. Han, S. M. Bak, J. Bai, X. Yu, H. Li and X. Q. Yang, *Nano Lett.*, 2016, **16**, 5999–6007.

40 S.-M. Bak, E. Hu, Y. Zhou, X. Yu, S. D. Senanayake, S.-J. Cho, K.-B. Kim, K. Y. Chung, X.-Q. Yang and K.-W. Nam, *ACS Appl. Mater. Interfaces*, 2014, **6**, 22594–22601.

41 S. Hwang, S. M. Kim, S.-M. Bak, B.-W. Cho, K. Y. Chung, J. Y. Lee, W. Chang and E. A. Stach, *ACS Appl. Mater. Interfaces*, 2014, **6**, 15140–15147.

42 H. Zhang, F. Omenya, M. S. Whittingham, C. Wang and G. Zhou, *ACS Energy Lett.*, 2017, **2**, 2598–2606.

43 L. Mu, R. Lin, R. Xu, L. Han, S. Xia, D. Sokaras, J. D. Steiner, T. C. Weng, D. Nordlund, M. M. Doeff, Y. Liu, K. Zhao, H. L. Xin and F. Lin, *Nano Lett.*, 2018, **18**, 3241–3249.

44 C. Wei, S. Xia, H. Huang, Y. Mao, P. Pianetta and Y. Liu, *Acc. Chem. Res.*, 2018, **51**, 2484–2492.

45 C. Wei, Y. Zhang, S.-J. Lee, L. Mu, J. Liu, C. Wang, Y. Yang, M. Doeff, P. Pianetta, D. Nordlund, X. Du, Y.-C. Tian, K. Zhao, J.-S. Lee, F. Lin and Y. Liu, *J. Mater. Chem. A*, 2018, **6**, 23055–23061.

46 P. C. Tsai, B. Wen, M. Wolfman, M. J. Choe, M. S. Pan, L. Su, K. Thornton, J. Cabana and Y. M. Chiang, *Energy Environ. Sci.*, 2018, **11**, 860–871.

47 C. Tian, Y. Xu, D. Nordlund, F. Lin, J. Liu, Z. Sun, Y. Liu and M. Doeff, *Joule*, 2018, **2**, 464–477.

48 J. Wandt, A. T. S. Freiberg, A. Ogrodnik and H. A. Gasteiger, *Mater. Today*, 2018, **21**, 825–833.

49 R. Jung, M. Metzger, F. Maglia, C. Stinner and H. A. Gasteiger, *J. Phys. Chem. Lett.*, 2017, **8**, 4820–4825.

50 B. Strehle, K. Kleiner, R. Jung, F. Chesneau, M. Mendez, H. A. Gasteiger and M. Piana, *J. Electrochem. Soc.*, 2017, **164**, A400–A406.

51 S.-K. Jung, H. Gwon, J. Hong, K.-Y. Park, D.-H. Seo, H. Kim, J. Hyun, W. Yang and K. Kang, *Adv. Energy Mater.*, 2014, **4**, 1300787.

52 F. Lin, I. M. Markus, D. Nordlund, T.-C. Weng, M. D. Asta, H. L. Xin and M. M. Doeff, *Nat. Commun.*, 2014, **5**, 3529.

53 F. Lin, D. Nordlund, I. M. Markus, T. C. Weng, H. L. Xin and M. M. Doeff, *Energy Environ. Sci.*, 2014, **7**, 3077–3085.

54 A. Manthiram, K. Chemelewski and E.-S. Lee, *Energy Environ. Sci.*, 2014, **7**, 1339–1350.

55 P. Mukherjee, N. V. Faenza, N. Pereira, J. Ciston, L. F. J. Piper, G. G. Amatucci and F. Cosandey, *Chem. Mater.*, 2018, **30**, 8431–8445.

56 K. Karki, Y. Huang, S. Hwang, A. D. Gamalski, M. S. Whittingham, G. Zhou and E. A. Stach, *ACS Appl. Mater. Interfaces*, 2016, **8**, 27762–27771.

57 P. Yan, J. Zheng, M. Gu, J. Xiao, J.-G. Zhang and C.-M. Wang, *Nat. Commun.*, 2017, **8**, 14101.

58 H. Zhang, K. Karki, Y. Huang, M. S. Whittingham, E. A. Stach and G. Zhou, *J. Phys. Chem. C*, 2017, **121**, 1421–1430.

59 S. Hwang, W. Chang, S. M. Kim, D. Su, D. H. Kim, J. Y. Lee, K. Y. Chung and E. A. Stach, *Chem. Mater.*, 2014, **26**, 1084–1092.

60 I. Arganda-Carreras, V. Kaynig, C. Rueden, K. W. Eliceiri, J. Schindelin, A. Cardona and H. Sebastian Seung, *Bioinformatics*, 2017, **33**, 2424–2426.

61 S. Webb, *Phys. Scr.*, 2005, **2005**, 1011.

62 Y. Liu, J. C. Andrews, J. Wang, F. Meirer, P. Zhu, Z. Wu and P. Pianetta, *Opt. Express*, 2011, **19**, 540–545.